Cross–diffusion based filtering as pre–processing step for remote sensing procedures

Eduardo Cuesta · Carmen Quintano · Alfonso Fernández–Manso

Abstract A new methodology combining 2×2 cross–diffusion systems of nonlinear partial differential equations (CDS) with classical image classification procedures is proposed in the present paper. Such a kind of mathematical models (CDS) have been theoretically studied in previous works in the context of image processing, however here they are tested and stressed in very practical instances. In particular, the main contribution of this paper is the improvement of the classification of satellite images when they are previously filtered by means of a CDS model. This conclusion is based on a wide and costly experimentation with satellite images of areas damaged by forest fires and surface coal mining, all of them located in Mediterranean areas. The efficiency of our methodology is not only in terms of the classification improvement but also in terms of the runtime saving since CDS based filtering is much less costly than other classical partial differential equations based filtering mathematical models as for example anisotropic models or higher order ones, always within the framework of nonlinear partial differential equations.

E. Cuesta (First author, Corresponding author)
Dept. of Applied Mathematics, E.T.S.I. of Telecommunication, Campus Miguel Delibes, University of Valladolid, Valladolid 47011, Spain. ORDID: 0000-0002-7508-6545. Tel.: +34-983423000. Fax: +34 983423661.
E-mail: eduardo@mat.uva.es

C. Quintano (Second author)
Electronic Technology Dept. and Sustainable Forest Management Research Institute (INIA), University of Valladolid, Valladolid 47014, Spain. ORDID: 0000-0001-6204-2319.
E-mail: menchu@tele.uva.es

A. Fernández–Manso (Third author)
Agrarian Sciences and Engineering Dept. University of León, León 24401, Spain. ORDID: 0000-0002-6255-5904.
E-mail: alfonso.manso@gmail.com

Keywords Cross–diffusion systems · Image filtering · Remote sensing

Mathematics Subject Classification (2010) MSC 68U10 · MSC 97M50

1 Introduction

Nonlinear Partial Differential Equatins (PDEs) based models for image processing were originally proposed by Perona–Malik in [36,37]. In those papers they considered convenient diffusion coefficients (so–called also *stopping functions*) allowing to handle the diffusion over the whole image by distinguishing parts of the image with different structure (flat, edges, corners,...). However the forward–backward parabolic character provided by these *stopping functions* may give rise to some theoretical drawbacks, in fact the ill– posedness of the associated initial and boundary value problem (IBVP), that is why more sophisticated PDEs based models have been later studied. In particular let us mention the pioneer paper of Catté et al. [8] where a regularization of the Perona–Malik model is stated, joint with the corresponding well–posedness of the associated IBVP. An extensive review of relevant approaches to mathematical models for image processing can be found in Weickert [43] and also in Aubert [4].

In the present paper we focus on a novel nonlinear PDEs based approach to image processing: Nonlinear parabolic 2×2 cross–diffusion systems. These models have been studied in connection to several practical applications, see e.g. Galiano et al. [15,16], or Ni [33], and recently they have been successfully applied for image restoration in Araújo et al. [2] where the authors state suitable assumptions on the diffusion matrix of the system to guarantee the well–posedness of

the cross–diffusion IBVP associated, as well as to ensure the compliance of a classical scale–space axiomatic, and the existence of Lyapunov functionals.

The main aim of this paper is to show that 2×2 cross–diffusion type systems, under the assumptions stated in [2], can play a crucial role in practical applications closely related to image processing, beyond some interesting theoretical properties already studied [29] and some others to be afforded in future papers. To this end we will focus on a particular image processing problem whose practical consequences are attracting the interest of many researchers in different fields (Engineers, Physicist, or Mathematicians): Achieving accurate estimations of earth areas damaged by natural phenomena (e.g. wildfires/forest fires [7,40]), or human–caused (e.g. surface coal mining [14,17,25,44]). This is a critical matter in order to evaluate economic losses, and to state convenient land recovering policies. In particular, it is very well known that forest fires are at present a very frequent phenomena all over the world and it may advocate to the desertification of big areas on the earth. Related to surface coal mining, several countries suffered such a kind of exploitation in an intensive manner for decades, and when the activity ended up this left a highly damaged landscape with multiple environmental consequences, among other, soil erosion and acidmine drainage. It is therefore clear that accurate estimations of damaged areas became a challenge for a sustainable development, to rehabilitate the affected landscapes, and to allow designing suitable environmental policies. This methodology could be used as well to others environmental degradations as e.g. crude oil leaks at sea, or even to medical imagery (TACs, MRIs, Scans,...).

Let us also highlight that other approaches have been proposed as well for similar purposes in the framework of remote sensing, just mention some, for example, the bilateral filters introduced by Aurich and Weule [5], and recently applied in the context of remote sensing by Kaplan et al. [23]. In spite of the simplicity of their formulation and implementation, some weakness have been reported, in fact this algorithm is highly runtime consuming since at each single position/pixel, the computation involves a weighted sum over a large neighboring pixels [34]. Moreover, filtering provided by this method is typically affected by the *stair case* phenomena as reported in [6].

In our study the proposed methodology uses as inputs some post–disturbance images of affected areas (by fires and surface coal mining) acquired by the Operational Land Imager (OLI) sensor on board of Landsat 8 satellite, and the Moderate Resolution Imaging Spectroradiometer (MODIS) sensor on board of Terra and Aqua satellites.

In the methodology we propose here every single image/input is considered as the initial data of the PDEs 2×2 based cross–diffusion system mentioned above, and they are evolved until a final time as a prior step to the classification of each pixel as *affected/non affected*. The resulting images of such a process turn out to be images whose inter–class variance increases, and the intra–class one decreases. In this manner it is expected to outperform the classification of inputs achieved by straightforward technics, i.e. without any prior *restoration*. This idea has been introduced in [39] where a nonlocal and linear PDEs based model of fractional type was considered, and later generalized to nonlocal linear models of Volterra type in [11]. However these models have several limitations: On the one hand the hight computational cost due to the memory effect, in fact the experiments carried out with these models in [11,39] have shown that runtime keeps far from real time performances; On the other hand the linearity of the models does not allows (in general) to state *filtering/restoration* criteria as sophisticated as with nonlinear models. The nonlinear and local model we propose here comes to address these issues.

Related to the classification, since the most important contribution of this paper is the use of the mathematical model mentioned above prior the classification process, we simply make use to classify every single pixel of the well known unsupervised algorithm *k–means* [27]. This algorithm defines a pre-determined number of clusters or classes within the satellite image that acts as input, assuming that: 1.-Class centre is defined by the arithmetic mean of all the points belonging to the class, and 2.-Each pixel is closer to its own class centre than to other class centres. Further and more recent reading on this algorithm can be found e.g. in [45] and references therein. Next, in order to group its different potential output classes into just our two classes of interest (*affected* and *non affected*) we follow a reclassification strategy which is mentioned in Section 3.

Finally an appropriate data assessment will allow us to identify the most accurate results as well as the optimal value of the parameters involved in the procedure. We used confusion matrixes where reference truth data were the rasterized perimeters of affected area. Note here that, since a large amount of experimental data are shown in the present paper, and in order to not extend unnecessarily the paper, no tables with comparison results are included, so we refer the reader to the papers cited above. With the same argument, and since the advantages are so obvious, nor comparative tables related to the efficiency in terms of the runtime, if compared to the methods considered in [11], are included.

The paper is organized as follows. In Section 2 the mathematical model is precisely described, both from the continuous and the numerical point of view. Section 3 is devoted to describe the original and synthetic bands to be classified, Section 4 describes the statistical methods for the accuracy assessment, and Section 5 shows several numerical experiments, and analyses the results in terms of statistical indexes described in the previous section. Finally in Section 6 we present some final conclusions and future papers.

2 Mathematical Model.

We devote this section to describe in detail the mathematical model we commented in Section 1 which is used at the filtering stage, and is prior to the pixels classification of the input images as *affected/non affected*. In particular in Sections 2.1 and 2.2 we describe the continuous IBVP and its fully discretization respectively.

2.1 Continuous Model

The evolutionary nonlinear IBVP we propose for the image restoration reads as the 2×2 coupled system of nonlinear partial differential equations,

$$\begin{cases} \dfrac{\partial u}{\partial t}(\mathbf{x},t) = \operatorname{div}\left(D_{11}(\mathbf{u}(\mathbf{x},t))\nabla u(\mathbf{x},t) \right. \\ \qquad\qquad \left. + D_{12}(\mathbf{u}(\mathbf{x},t))\nabla v(\mathbf{x},t)\right), \\ \dfrac{\partial v}{\partial t}(\mathbf{x},t) = \operatorname{div}\left(D_{21}(\mathbf{u}(\mathbf{x},t))\nabla u(\mathbf{x},t) \right. \\ \qquad\qquad \left. + D_{22}(\mathbf{u}(\mathbf{x},t))\nabla v(\mathbf{x},t)\right), \end{cases} \tag{1}$$

for $(\mathbf{x},t) \in \Omega \times [0,T]$, where,

$$\mathbf{u} : \Omega \times [0,T] \longrightarrow \mathbb{R}^2$$
$$(\mathbf{x},t) = (x,y,t) \;\mapsto\; \mathbf{u}(\mathbf{x},t) = (u(x,y,t), v(x,y,t))^T,$$

and $\Omega \subset \mathbb{R}^2$. Typically Ω stands for a square domain, in particular, for the sake of the simplicity of the notation, from now on we will assume that $\Omega = [0,L] \times [0,L]$, $L > 0$. Moreover, $D_{ij} : \mathbb{R}^2 \to \mathbb{R}$, $i,j = 1,2$, stand for the diffusion coefficients, and the operators div, and ∇ are the divergence and gradient operators respectively. In addition we set the initial conditions $\mathbf{u}_0 = (u_0, v_0)$ where,

$$\mathbf{u}_0(\mathbf{x}) = (u(\mathbf{x},0), v(\mathbf{x},0))^T = (u_0(\mathbf{x}), v_0(\mathbf{x}))^T, \tag{2}$$

for $\mathbf{x} \in \Omega$, and the homogeneous Neumann boundary conditions as follows,

$$\begin{aligned} &\langle D_{11}(\mathbf{u}(\mathbf{x},t))\nabla u(\mathbf{x},t) + D_{12}(\mathbf{u}(\mathbf{x},t))\nabla v(\mathbf{x},t), \mathbf{n}\rangle = 0, \\ &\langle D_{21}(\mathbf{u}(\mathbf{x},t))\nabla u(\mathbf{x},t) + D_{22}(\mathbf{u}(\mathbf{x},t))\nabla v(\mathbf{x},t), \mathbf{n}\rangle = 0, \end{aligned} \tag{3}$$

for $(\mathbf{x},t) \in \partial\Omega \times [0,T]$, where $\partial\Omega$ stands for the boundary of Ω, $\langle \cdot, \cdot \rangle$ denotes the Euclidean inner product, and $\mathbf{n}$ the outward normal vector on $\partial\Omega$. Recall that given two vectors $\mathbf{a} = (a_1, \ldots, a_n)$ and $\mathbf{b} = (b_1, \ldots, b_n)$, the scalar product is defined by $\langle \mathbf{a}, \mathbf{b} \rangle = \sum_{j=1}^{n} a_j b_j$.

The application of (1)–(3) to image processing requires some explanations before being implemented. In particular related to the initial data we must point out that in classical PDEs based approaches to image processing, the original image (probably perturbed/ damaged/ noisy/ ...) usually plays the role of the initial data of the evolutionary model, however in (1)–(3) the initial data has two components u_0 and v_0. Different distributions u_0 and v_0 are in fact admissible, however a depth discussion on the results achieved depending on such a choice is out of the scope of this work, therefore we state a naive choice of the initial data $\mathbf{u}_0$ consisting on u_0 simply standing for the original image, and $v_0 \equiv 0$. This choice is not by chance, in fact this choice of $\mathbf{u}_0$ was proposed by Gilboa et al. in [18] in the framework of nonlinear complex diffusion for image processing. This fact has been discussed in more depth in [2]. Moreover, we briefly comment on the well–posedness of (1)–(3), in particular denote the diffusion matrix of (1), $D(\mathbf{u}) : \overline{\Omega} \times [0,T] \to \mathcal{M}_{2\times 2}(\mathbb{R})$,

$$D(\mathbf{u})(\mathbf{x},t) := D(\mathbf{u}(\mathbf{x},t)) = \begin{pmatrix} D_{11}(\mathbf{u}(\mathbf{x},t)) & D_{12}(\mathbf{u}(\mathbf{x},t)) \\ D_{21}(\mathbf{u}(\mathbf{x},t)) & D_{22}(\mathbf{u}(\mathbf{x},t)) \end{pmatrix},$$

where $\overline{\Omega}$ stands for the closure of Ω. Therefore, if D is uniformly positive definite , and their entries $D_{i,j}$, $j = 1,2$, are the Lipschitz continuous and global bounded, then the problem (1)–(3) turns out to be well–posed (existence and uniqueness of a weak solution), including the continuous dependence of the initial data, and the existence of an extremum principle. Consequently (1)–(3) admits a continuous evolution operator T_t, so–called *space–scale operator*, such that if $\mathbf{u}$ stands for its solution, then we have the (space–scale) representation

$$T_t : \mathbf{u}_0(\cdot) \to T_t(\mathbf{u}_0(\cdot)) = \mathbf{u}(\cdot, t).$$

Other relevant properties of the solution of (1)–(3), in particular most of classical space–scale properties (Grey–level shift invariance; Reverse contrast invariance;...) might be under certain additional requirements for D, are precisely studied in [2].

Related to the matrix diffusion it has been reported in [2] that slightly different results can be achieved depending on the choice of D, always within the framework of assumptions stated in [2]. In fact, according the criteria in [1] and [18] a convenient matrix D has the

following form

$$D(\mathbf{u}) = D(u, v) = g(|v_\sigma|)d, \tag{4}$$

where

$$g(w) := \frac{1}{1 + \frac{|w|^2}{\nu}},$$

with ν standing for a threshold parameter, v_σ represents the second component of a Gaussian regularization of $\mathbf{u}$, and

$$d := \begin{pmatrix} d_{11} & d_{12} \\ d_{21} & d_{22} \end{pmatrix}, \ d_{ij} \in \mathbb{R},$$

is a positive definite matrix.

Note that the function g depends solely on the (regularized) second component of $\mathbf{u}$ (see (4)), following the ideas of Gilboa et al. [18], and in particular the property so–called *small theta approximation* for complex diffusion models. In fact, the numerical experiments of Section 5 have been carried out with the threshold $\nu = 10$, and the Gaussian deviation $\sigma = 10^{-2}$. That choice is suggested by the experiments in [2] where this values (among the other parameters involved) led to the good performance shown there.

A convenient choice of the diffusion matrix D according the previous comment and assumptions in [2], leads to a two–components solution $\mathbf{u}$ of (1)–(3) where the first component represents the evolved initial data (original image) u_0 along the time interval $0 \leq t \leq T$, which means a restoration of the original image, and the second component of $\mathbf{u}$ stands for the evolution of some feature of the original image. Typically the second component plays the role of an edge detector, helping the diffusion process to preserve shapes, and in particular edges and corners. This property arises from the complex diffusion model considered in [18] where the imaginary part of their solution, if the imaginary part of the complex diffusion coefficient is small (in fact, though as a limit), behaves like a scaled smoothed Gaussian derivative of the original image. Here the function v, i.e. the second component of $\mathbf{u}$, plays the role of the imaginary part in [18] thought the cross–diffusion models as a generalization of the complex diffusion ones.

Finally let us highlight that several choices of the matrix d (i.e. the matrix D according to (4)) satisfying the requirements mentioned above have been experimented in [2], and those results led us to conclude that a convenient choice of d for our experiments is (NCDF1 according the notation in [2])

$$d = \begin{pmatrix} 1.000 & 0.025 \\ 1.000 & 1.000 \end{pmatrix}.$$

2.2 Fully Discrete Model

The implementation of (1)–(3) is carried out by suitable time and space discretizations. Notice that since the order of convergence is not a crucial matter here we simply combines a first order in time discretization based on the explicit Euler method, and a second order in space difference scheme.

Let Ω_h be an uniform spatial mesh of size $h > 0$,

$$\Omega_h = \{\mathbf{x}_{ij} = (ih, jh) \in \Omega : 0 \leq i, j \leq N\},$$

where in fact $h = L/N$, for an integer $N > 0$. Besides, let M be the number of time steps for the time discretization. Hence, for $\tau = T/M$, denote $t_m = m\tau$, $0 \leq m \leq M$.

Denote also $U^0 = (U^0_{i,j})_{0 \leq i,j \leq N}$, and $V^0 = (V^0_{i,j})_{0 \leq i,j \leq N}$, the $N \times N$ matrices corresponding to the initial data in Ω_h where $U^0_{i,j} = u_0(\mathbf{x}_{ij})$ and $V^0_{i,j} = v_0(\mathbf{x}_{ij})$, and $U^m = (U^m_{i,j})_{0 \leq i,j \leq N}$ and $V^m = (V^m_{i,j})_{0 \leq i,j \leq N}$, the matrices whose entries correspond to the approximations of $\mathbf{u}(\mathbf{x}_{ij}, t_m)$ provided by the fully discrete scheme considered in [2] (formula (3.5)), here element–wise written as follows

$$\begin{aligned}
&\frac{U^{m+1}_{i,j} - U^m_{i,j}}{\tau} = \\
&= \frac{1}{2h}\Bigg\{ g(V^m_{i+1,j}) \left(d_{11} \frac{U^m_{i+2,j} - U^m_{i,j}}{2h} + d_{12} \frac{V^m_{i+2,j} - V^m_{i,j}}{2h} \right) \\
&\quad - g(V^m_{i-1,j}) \left(d_{11} \frac{U^m_{i,j} - U^m_{i-2,j}}{2h} + d_{12} \frac{V^m_{i,j} - V^m_{i-2,j}}{2h} \right) \\
&\quad + g(V^m_{i+1,j}) \left(d_{11} \frac{U^m_{i,j+2} - U^m_{i,j}}{2h} + d_{12} \frac{V^m_{i,j+2} - V^m_{i,j}}{2h} \right) \\
&\quad - g(V^m_{i-1,j}) \left(d_{11} \frac{U^m_{i,j} - U^m_{i,j-2}}{2h} + d_{12} \frac{V^m_{i,j} - V^m_{i,j-2}}{2h} \right) \Bigg\} \\
&\frac{V^{m+1}_{i,j} - V^m_{i,j}}{\tau} = \\
&= \frac{1}{2h}\Bigg\{ g(V^m_{i+1,j}) \left(d_{21} \frac{U^m_{i+2,j} - U^m_{i,j}}{2h} + d_{22} \frac{V^m_{i+2,j} - V^m_{i,j}}{2h} \right) \\
&\quad - g(V^m_{i-1,j}) \left(d_{21} \frac{U^m_{i,j} - U^m_{i-2,j}}{2h} + d_{22} \frac{V^m_{i,j} - V^m_{i-2,j}}{2h} \right) \\
&\quad + g(V^m_{i+1,j}) \left(d_{21} \frac{U^m_{i,j+2} - U^m_{i,j}}{2h} + d_{22} \frac{V^m_{i,j+2} - V^m_{i,j}}{2h} \right) \\
&\quad - g(V^m_{i-1,j}) \left(d_{21} \frac{U^m_{i,j} - U^m_{i,j-2}}{2h} + d_{22} \frac{V^m_{i,j} - V^m_{i,j-2}}{2h} \right) \Bigg\},
\end{aligned} \tag{5}$$

for $0 \leq m \leq M - 1$, and $0 \leq i, j \leq N$.

Finally the discrete homogeneous Newmann boundary conditions are given in a classical manner, taking also into account that spatial discretization is based on a $2h$–length finite differences scheme (see [2] for more details).

Note that the numerical scheme (5) is explicit and some restriction related to the time step, i.e. some stability condition, is expected to be requiered. In fact, under the assumptions stated in [2] for the matrix diffusion D, it is feasible to extend the stability condition (2.35) obtained in [3] for complex diffusion models, (or (3.6) in [2]) to the numerical scheme (5). Since further analysis on the stability issues is out of the scope of this paper, we admit that this condition applies for (5), and that the choice of the time step $\tau = 0.05$ and the size of the mesh grid $h = 1$ (normalized without lost of generality) in Section 5 largely satisfy that condition.

3 Satellite imagery and *k*–means algorithm

Traditionally, damaged areas were mapped by fieldwork, although currently satellite data are widely used to map the extent of affected areas. In particular mapping burned areas we present here makes use of the coarse spatial resolution imagery provided by the MODIS sensor launched in 1999 and 2002 on board the Terra and Aqua satellites, respectively. In the same manner the study of surface coal mining degraded areas we show here is based on the OLI sensor on board of Landsat 8 satellite, that offers moderate to high spatial resolution at no charge since 2008.

The details of the bands and wavelength provided by MODIS and OLI sensors and Landsat satellite are shown in Table 1.

3.1 Forest fires

We carried out our experimentation for forest fires occurred in Mediterranean countries in fact in Spain, where statistical analyses reveal a pattern of great concentration of the total burned area in a relatively small number of large fires [7]. It has been studied [13,19,24] that B_{NIR} is more sensitive to the existence of living vegetation, and the B_{SWIR3} is more sensitive to the existence of charred post–fire organic material, therefore they seem to be the most convenient bands to define accurate indexes to classify burned areas.

In particular the so–called vegetation indexes are indexes though to enhance living vegetation signals and minimize the background noise due to soil and atmospheric effects, and they are typically based on the spectral difference between two spectral bands, B_{Red} and B_{NIR}. In this we consider some of the most common vegetation indexes used in the literature (see Table 2). However these indexes have general purposes beyond the specific one of burned area mapping, and in fact they only involve red and near–infrared (NIR) bands for their definitions. That is why we also consider in our analysis other vegetation indexes thought specifically for burned area mapping. In particular we consider the indexes in Table 3, where we note that their definitions mainly involve B_{NIR} and B_{SWIR3}. Let us highlight that we consider in our study the index NBR which is probably the most applied burn severity index, together with its corresponding differenced index (dNBR) [31].

3.2 Surface coal mining

Once again both, original bands and vegetation indexes, take part of a common methodology for accurate mapping of surface coal mining degraded areas (see e.g. [20]). It is well known that almost all vegetation indexes display an important decrease in surface coal mining affected areas if compared to vegetated unaffected ones. NDVI can be considered also here as a reference, however, in areas where the rate of soil surface exposed is high (higher than 50%) the reflectance of light on the red and NIR band can affect vegetation index values. Specific vegetation indexes have been consider in the literature as the ones described in Table 4

Let us mention that index SAVI stands for a modification of the NDVI defined in Table 2 that corrects the influence of soil brightness when vegetative cover is low, and the environment is a mixture of soil types. On the other hand indexes MSAVI and MSAVI2 are further modifications of index SAVI.

3.3 Classification algorithm

In order to automatize as much as possible the procedure of classification, we consider in this an unsupervised classifier, i.e. no initializing cluster centers have to be provided by the user. To this end we made use of the well known unsupervised *k–means* algorithm [26] (Matlab© software package). A refinement of this algorithm is implemented here as in [11,39]. It consists in: 1.- A first classification ranging between 3 and 10 classes; 2.- A second classification of each of them in merely two classes, *affected* or *not affected*, both steps computed by means of the *k–means* algorithm following the criteria in [11]. Note that no more sophisticated classifier has been considered because the main contribution of this is to show how a convenient filtering prior to the classification helps to improve the accuracy of the results provided by the classifier himself.

		Landsat OLI	MODIS
Spectral resolution (wavelenght range in μmeters)	B_{Blue}	$0.450 - 0.515$	$0.459 - 0.479$
	B_{Green}	$0.525 - 0.605$	$0.545 - 0.565$
	B_{Red}	$0.630 - 0.680$	$0.620 - 0.670$
	B_{NIR}	$0.845 - 0.885$	$0.841 - 0.876$
	B_{SWIR1}	–	$1.230 - 1.250$
	B_{SWIR2}	$1.560 - 1.650$	$1.628 - 1.652$
	B_{SWIR3}	$2.100 - 2.300$	$2.105 - 2.155$
Spatial resolution (meters)		30	250, B_{Red} and B_{NIR} 500 the rest
Temporal resolution (days)		16	$1 - 2$

Table 1 Landsat 8 OLI, and MODIS reflective bands. B_{Blue}: Blue band; B_{Green}: Green band; B_{Red}: Red band; B_{NIR}: Near–Infrared band; B_{SWIR}: Short Wave Infrared 1, 2, and 3 bands

Normalized Difference Vegetation Index (NDVI) see [42]	$\text{NDVI} = \frac{B_{NIR} - B_{Red}}{B_{NIR} + B_{Red}}$
Global Environment Monitoring Index (GEMI) see [35]	$\text{GEMI}= \nu\,(1 - 0.25\nu) - \frac{B_{Red} - 0.125}{1 - B_{Red}}$
Enhance Vegetation Index (EVI) see [21]	$\text{EVI}= G\,\frac{B_{NIR} - B_{Red}}{B_{NIR} + C_1 B_{Red} - C_2 B_{Blue} + L}$

Table 2 Common vegetation indexes. $\nu = \frac{2(B_{NIR}^2 - B_{Red}^2) + 1.5B_{NIR} + 0.5B_{Red}}{B_{NIR} - B_{Red} + 0.5}$, $G = 2.5$ gain factor; $C_1 = 6$; $C_2 = 7.5$; and $L = 1$.

Normalized Burn ratio (NBR) see [28]	$\text{NBR} := \frac{B_{NIR} - B_{SWIR3}}{B_{NIR} + B_{SWIR3}}$
Burned Area Index (BAI) see [9]	$\text{BAI}:= \frac{1}{(0.06 - B_{NIR})^2 + (0.1 - B_{Red})^2}$
Burned Area Index adapted to MODIS (BAIM) see [30]	$\text{BAIM}:= \frac{1}{(0.05 - B_{NIR})^2 + (0.2 - B_{SWIR3})^2}$

Table 3 Spectral indexes oriented to map burned areas.

4 Accuracy Assessment

The most recommended approaches to measure the accuracy of classification procedures are the confusion matrix, and κ statistic [10]. Recall, the confusion matrix is a 2×2 matrix that accounts the positives (*affected* pixels) or negatives (*non affected pixels*), correctly or not correctly classified, in the following manner

$$\begin{pmatrix} m_{11} = \#\text{True } \textit{affect.} & m_{12} = \#\text{False } \textit{affect.} \\ m_{21} = \#\text{False } \textit{non affect.} & m_{22} = \#\text{True } \textit{non affect.} \end{pmatrix}. \tag{6}$$

Moreover κ statistic defines as

$$\kappa := 1 - \frac{1 - P(a)}{1 - P(e)}, \tag{7}$$

where,

- $P(a) := p_{11} + p_{22}$, stands for the probability of agreement (true *affected* + true *non affected*), with

$$p_{ij} = \frac{m_{ij}}{m_{11} + m_{12} + m_{21} + m_{22}}, \quad i, j = 1, 2.$$

- $P(e) := P_1 + P_2$ where,

$$P_1 := (p_{11} + p_{12})\,(p_{11} + p_{21})\,,$$

and

$$P_2 := (p_{21} + p_{22})\,(p_{12} + p_{22})\,.$$

Note that P_1 stands for the probability of true and simultaneously *affected*, and similarly P_2 stands for the probability of false and simultaneously *non affected*. Therefore $P(e)$ represents the probability of random agreement.

It has been reported the interest of considering disproportional samplings prior the confusion matrix computation [41]. In fact, a stratified random disproportional sampling consisting in 80% of the validating pixels located on the affected areas, and the rest (20%) on unaffected areas have been applied in our experiments.

The McNemar test [12] is used to predict the statistical significance of the difference in accuracy between two classifications with κ statistics estimated from the same or related samples. This test acts on the confusion

Soil–Adjusted Vegetation Index (SAVI) see [22]	$\text{SAVI} := \frac{1.5(\text{B}_{\text{NIR}} - \text{B}_{\text{Red}})}{\text{B}_{\text{NIR}} + \text{B}_{\text{Red}} + 0.5}$
Modified Soil-Adjusted Vegetation Index 2 (MSAVI2, often MSAVI) see [38]	$\text{MSAVI2:}= \frac{2\text{B}_{\text{NIR}} + 1 - \sqrt{(2\text{B}_{\text{NIR}} + 1)^2 - 8(\text{B}_{\text{NIR}} - \text{B}_{\text{Red}})}}{2}$

Table 4 Spectral indexes oriented to map degraded areas by coal mining

matrix (6), and is based on the *chi square* test, i.e. χ^2 test,

$$\chi^2 = \frac{(m_{12} - m_{21})^2}{m_{12} + m_{21}}.$$

With a sufficiently large number of discordant data ($m_{12}, m_{21} >> 0$), χ^2 has a *chi–squared* distribution with 1 degree of freedom, and in our case this test helps us to determine whether the accuracy difference of estimates obtained for damaged areas, with and without previous filtering, has statistical significance. Note that the McNemar test, with continuity correction [12], gives $\chi^2_c = 3.84$ with 95% statistical significance, and the null hypothesis is rejected if $\chi^2 > \chi^2_c$.

Finally, note that we consider as reference truth for the burned areas experiments the official burned area perimeters, and for the surface coal mining damaged area mapping experiment, the perimeters digitized over ortho–photographs (50 cm).

5 Numerical Experiments

This section is devoted to present some practical experiments according the methodology described in previous sections. In fact, we classify satellite images corresponding to areas affected by forest fires and areas affected by coal mining, but previously applying to every single input image a filtering based on the (continuous) mathematical model (1)–(3) and its numerical discretization (5), according to the parameters stated in Section 2.

First of all, we show in Sections 5.1 and 5.2 additional information, i.e. not previously provided, related to the numerical experiments carried out, and we conclude with the Section 5.3 where we include several comments on the results obtained.

5.1 Study Areas

To illustrate the outperformance of the proposed methodology we consider several damaged areas located Spain. In fact, Table 5 describes the four burned study areas considered in this , all of them located in the Northern Spain. The MOD13Q1 product provides two primary vegetation layers, NDVI and EVI. Along with the vegetation layers it includes MODIS Reflectance bands R_{Red}, R_{NIR}, R_{Blue}, and R_{SWIR1}. All the layers are resampled to 250m.

Burned area perimeters measured on the ground from helicopters by GPS, and provided by the Autonomous Community of Castilla y León government (Spain), were used as reference truth.

The surface coal mining damaged areas considered for our experiments are described in Table 6, all of them also located in Spain (Northern–Western).

A Landsat 8 Operational Land Imager (OLI) scene (path 2013, row 30), acquired on June 29, 2013, and downloaded from US Geological Survey (USGS) (www.glovis.usgs.gov) was used. An ortho–photograph subsequent to surface coal mining activities was used to validate the surface coal mining affected area estimates. Specifically, we used a 50cm ortho–photograph from the Spanish National Center of Geographic Information (CNIG;
http://www.cnig.es/). It was recorded in summer 2013 in the frame of the Spanish Aerial Ortho–photography National Planning (PNOA).

5.2 Numerical results

The stability condition for the numerical scheme mentioned in Section 2.2 is here taken into account to set the time and space mesh lengths. In fact we consider $h = 1$ (without loss of generality), and $\tau = 0.05$ (with final time $T = 5$), and therefore fulfilling such a condition.

The parameters involved in the experiments appeared in Tables 1–8 are:

- I stands for the time step of the time discretization where the best result is reached.
- C and RC represent the classes and re–classes according the criteria commented in Section 4.
- McN stands for the McNemar test values.
- And finally, UA, PA, and OA stand for the User Accuracy, Producer Accuracy, and Omission Accuracy respectively.

In Tables 1–8 we show the best values of κ (first line), $\%\kappa$ represents the improvement of κ (in %) of filtered input with respect to the non–filtered one (second line), McNemar test (third line), User Accuracy,

Study area	Fire date	Burned area (km^2)	Forest species
Zamora (1)	17 July 2004	23.8	*Quercus ilex L., Quercus pyrenaica Willd, Citrus.*
Zamora (2)	24 August 2008	2.6	Non–forested and *Pinus pinaster and Quercus pyrenaica.*
Burgos	31 July 2008	9.0	Non–forested.
Segovia	6 August 2008	9.9	*Pinus pinaster Ait., Pinus nigra Arn.*

Table 5 Study areas for burned areas mapping experiement.

Disctric	Mine name	Damaged area (km^2)
Degaña	Cerredo	3.17
Villablino (1)	Fonfría	2.35
Villablino (2)	Feixolín	1.91
Cabrillanes	Nueva Julia	3.41

Table 6 Study areas for surface coal mining damaged areas mapping experiment.

Producer Accuracy, and Omission Accuracy (fourth to sixth lines), and the values of I, C and RC where the best results are reached (last line), for different instances:

- For burned area mapping (Tables 1–4) we show the best values for the vegetation indexes EVI, GEMI, BAI, BAIM, and NBR, and for surface coal mining mapping (Tables 5–8) the best values of the original bands B_{Red}, B_{NIR}, and B_{SWIR3}, and the vegetation indexes MSAVI and NDVI. In both cases the best value of bands and vegetation indexes are chosen in terms of the optimal κ, and for each of them with and without filtering (first and second five–column blocks for each table respectively). In case of filtering I indicates the time level where the best value is reached. Obviously no filtering means that $I = 0$. The parameters C and RC indicate the number of classes and re–classes for which the best value is reached.
- The third five–columns block show the best values of bands and vegetation indexes in terms of the optimal time iteration according the criteria stated in [32]. Recall that this criteria provides the iteration where the image optimal restoration is reached in terms of the correlation coefficient of $U^0 - U^m$ and the original image U^0. In fact this criteria states that the optimal iteration is computed as follows,

$$I_{opt} := \min \left\{ m : \mathrm{corr}(U^0 - U^m, U^m) \text{reachs the min., for } 1 \le m \le M \right\}, \quad (8)$$

where the correlation between two images U_1 and U_2 is defined as

$$\mathrm{corr}(U_1, U_2) := \frac{\langle U_1 - \bar{U}_1, U_2 - \bar{U}_2 \rangle_F}{\|U_1 - \bar{U}_1\|_F \|U_2 - \bar{U}_2\|_F}$$

being $\langle \cdot, \cdot \rangle_F$ the Frobenius inner product, $\| \cdot \|_F$ the associated norm, and $\bar{U}_j$ the constant image with all intensities equal to the intensities mean value, $j = 1, 2$.

The Figures shown in the present have been generated by Matlab©, R2014b release.

In Figures 1–6 we visually illustrate some of the numerical results of Tables 1–8. Every single eight–block figures represents from left to right, and from top to bottom: The original input; the filtered one according the best κ; the filtered input according the optimal time; the curve of correlation according (8) with the optimal time (circle) and the optimal κ (solid dot); the ground truth; classification for the best κ; classification for the optimal time; and classification without filtering.

Figures 1–2 intend to show that under a threshold size of the affected area classification becomes less and less accurate, even worse after filtering. On the contrary, under some size Figures 3–4 show that the filtering procedure (in terms of the optimal κ and the optimal time) outperforms the results of the classification himself, in fact it can be observed that isolated patches are completely removed. Finally Figures 5–6 are intended to show, in addition to the classification improvement, that the optimal time is not always reached at last time step, on the contrary depending of the features of the image it can be reached at early steps. Observe anyhow that best κ is always reached before the optimal time.

Table 1. 1st Forest fire: Zamora (1), July 2004 (see Section 5.2 for detailed description)

		Best κ										Optimal Time				
		Filtered					Non Filtered									
Indexes		EVI	GEMI	BAI	BAIM	NBR	EVI	GEMI	BAI	BAIM	NBR	EVI	GEMI	BAI	BAIM	NBR
κ		0.76	0.85	**0.86**	0.84	0.84	0.67	**0.79**	**0.79**	0.78	0.77	0.70	0.82	**0.83**	**0.83**	0.82
κ (%)		13.4	7.5	8.8	7.6	9.0	-	-	-	-	-	4.4	3.7	5.0	6.4	6.4
McN.		253	216	182	174	204	-	-	-	-	-	268	21	171	186	189
UA (%)		92.2	97.8	97.3	97.2	97.0	94.8	96.1	96.8	96.2	95.9	95.0	97.0	97.1	97.0	97.0
PA (%)		96.0	98.2	98.4	97.9	98.1	95.0	97.7	96.4	97.3	97.2	95.8	97.3	98.4	97.7	97.2
OA (%)		94.1	96.5	96.8	96.2	96.3	92.2	95.3	94.9	95.0	94.7	93.0	95.7	95.8	96.0	95.6
Opt. Param.	I	23	39	18	61	23	-	-	-	-	-	99	95	93	97	83
	C	5	5	5	5	5	7	6	5	6	6	5	5	5	5	5
	RC	1	1	1	1	1	1	1	1	1	1	1	1	1	1	1

Table 2. 2nd Forest fire: Zamora (2), August 2008 (see Section 5.2 for detailed description)

		Best κ										Optimal Time				
		Filtered					Non Filtered									
Indexes		EVI	GEMI	BAI	BAIM	NBR	EVI	GEMI	BAI	BAIM	NBR	EVI	GEMI	BAI	BAIM	NBR
κ		0.18	**0.82**	0.73	0.79	0.79	0.12	**0.75**	0.67	0.72	0.74	0.10	0.40	0.43	**0.47**	0.44
κ (%)		50.0	9.3	8.9	9.7	6.7	-	-	-	-	-	-16.7	-46.7	-35.9	-34.8	-40.6
McN.		183	276	20	17	16	-	-	-	-	-	373	358	27	30	21
UA (%)		96.7	99.6	99.4	99.4	99.5	92.8	99.3	99.1	99.2	99.3	93.7	99.0	99.1	99.3	99.1
PA (%)		86.8	99.5	99.1	99.5	99.4	79.6	99.4	99.0	99.4	99.4	81.5	95.0	95.4	96.2	95.8
OA (%)		86.5	99.1	98.6	99.0	99.0	79.7	98.8	98.3	98.6	99.4	81.0	94.7	95.0	95.8	95.4
Opt. Param.	I	1	6	6	6	6	-	-	-	-	-	100	99	100	100	100
	C	10	9	10	10	10	10	10	9	10	10	9	10	10	10	10
	RC	1	1	1	1	1	1	1	1	1	1	1	1	1	1	1

Table 4. 4th Forest fire: Segovia, August 2008 (see Section 5.2 for detailed description)

		Best κ										Optimal Time				
		Filtered					Non Filtered									
Indexes		EVI	GEMI	BAI	BAIM	NBR	EVI	GEMI	BAI	BAIM	NBR	EVI	GEMI	BAI	BAIM	NBR
κ		0.33	**0.59**	**0.59**	0.57	**0.59**	0.32	**0.54**	0.53	0.53	0.52	0.09	**0.34**	0.33	0.32	**0.34**
κ (%)		3.1	9.2	11.3	7.5	13.4	-	-	-	-	-	-61.9	-37.1	-37.8	-39.7	-34.7
McN.		48	82	20	26	52	-	-	-	-	-	166	112	110	90	93
UA (%)		94.2	95.7	96.2	95.9	95.7	94.1	95.9	95.7	95.6	94.8	82.5	94.3	94.1	94.1	94.2
PA (%)		94.0	98.5	97.2	97.5	98.5	93.6	96.4	96.5	97.1	99.2	72.4	90.2	89.4	89.9	90.3
OA (%)		90.0	94.9	94.4	94.3	94.9	89.6	93.5	93.4	93.7	94.7	70.6	87.5	86.8	87.1	87.5
Opt. Param.	I	2	2	9	9	8	-	-	-	-	-	100	100	99	100	100
	C	10	7	8	8	8	10	6	6	6	9	10	10	10	10	10
	RC	1	1	1	1	1	1	1	1	1	1	1	1	1	1	1

Table 3. 3rd Forest fire: Burgos, July 2008 (see Section 5.2 for detailed description)

		Best κ										Optimal Time				
		Filtered					Non Filtered									
Indexes		EVI	GEMI	BAI	BAIM	NBR	EVI	GEMI	BAI	BAIM	NBR	EVI	GEMI	BAI	BAIM	NBR
κ		0.75	**0.94**	0.92	0.93	0.92	0.70	**0.82**	0.81	0.79	0.79	0.29	**0.92**	0.87	0.91	0.90
κ (%)		7.1	14.6	13.5	17.7	16.4	-	-	-	-	-	-58.6	12.1	7.4	15.1	13.9
McN.		576	638	643	3	4	-	-	-	-	-	252	2	30	7	5
UA (%)		97.0	99.4	99.3	99.6	99.6	96.5	97.7	97.8	97.5	97.3	91.6	99.7	99.5	99.8	99.6
PA (%)		99.6	99.5	99.3	99.0	99.0	99.4	99.6	99.2	99.4	99.7	81.8	98.9	98.1	98.6	98.6
OA (%)		97.0	99.0	98.9	98.9	99.0	96.4	97.7	97.5	97.3	97.4	81.0	98.8	98.0	98.6	98.5
Opt. Param.	I	7	16	11	73	73	-	-	-	-	-	100	86	100	100	100
	C	6	4	4	6	6	9	5	5	5	6	10	6	7	6	7
	RC	1	1	1	1	1	1	1	1	1	1	1	1	1	1	1

Table 5. 1st Disctric: Degaña; Mine: Cerredo (see Section 5.2 for detailed description)

		Best κ										Optimal Time				
		Filtered					Non Filtered									
Indexes		B_{Red}	B_{NIR}	B_{SWIR3}	MSAVI	NDVI	B_{Red}	B_{NIR}	B_{SWIR3}	MSAVI	NDVI	B_{Red}	B_{NIR}	B_{SWIR3}	MSAVI	NDVI
κ		0.89	0.80	0.67	**0.94**	**0.94**	0.83	0.78	0.64	**0.92**	0.91	0.88	0.76	0.65	**0.88**	0.87
κ (%)		7.2	2.5	4.6	2.1	3.2	-	-	-	-	-	6.0	-2.6	1.5	-4.4	-4.4
McN.		170	51	38	38	66	-	-	-	-	-	92	114	84	57	61
UA (%)		94.9	90.9	84.8	97.1	96.9	92.4	90.1	83.7	96.4	96.2	94.3	88.6	83.9	94.1	93.7
PA (%)		94.9	90.7	86.4	97.4	97.4	92.7	90.1	85.3	96.9	96.5	94.8	90.8	85.7	96.9	95.0
OA (%)		94.6	90.3	84.7	97.1	97.0	92.2	89.6	83.5	96.5	96.1	94.2	89.0	83.8	94.6	94.0
Opt. Param.	I	22	5	16	2	2	-	-	-	-	-	35	64	51	23	31
	C	4	10	9	9	8	6	7	8	9	8	7	7	5	9	10
	RC	2	3	4	4	3	3	2	4	4	3	3	2	2	4	4

Table 6. 2nd Disctric: Villablino; Mine Fonfría (see Section 5.2 for detailed description)

		Best κ										Optimal Time				
		Filtered					Non Filtered									
Indexes		B_{Red}	B_{NIR}	B_{SWIR3}	MSAVI	NDVI	B_{Red}	B_{NIR}	B_{SWIR3}	MSAVI	NDVI	B_{Red}	B_{NIR}	B_{SWIR3}	MSAVI	NDVI
κ		0.93	0.79	0.80	**0.95**	0.94	0.87	0.78	0.61	**0.93**	**0.93**	0.91	0.75	0.80	**0.92**	0.90
κ (%)		6.8	1.2	31.1	2.1	1.0	-	-	-	-	-	4.5	-3.9	31.1	-1.1	-3.3
McN.		201	27	503	43	43	-	-	-	-	-	218	124	503	97	401
UA (%)		96.4	89.3	90.0	97.3	97.1	93.8	89.0	80.9	96.8	96.8	95.5	87.6	90.0	96.0	94.4
PA (%)		96.4	90.1	90.4	97.5	97.2	93.9	89.6	81.0	97.0	97.0	95.8	87.5	90.4	96.9	95.1
OA (%)		96.4	89.8	90.2	97.4	97.2	93.8	89.3	80.9	96.9	96.9	95.7	87.5	90.1	96.8	95.0
Opt. Param.	I	12	4	100	2	2	-	-	-	-	-	27	20	100	13	15
	C	6	8	6	4	9	6	8	7	10	6	7	10	6	9	8
	RC	3	2	3	2	3	3	2	4	4	2	3	3	3	4	3

Table 8. 4th Disctric: Cabrillanes, Mine Nueva Julia (see Section 5.2 for detailed description)

		Best κ										Optimal Time				
		Filtered					Non Filtered									
Indexes		B_{Red}	B_{NIR}	B_{SWIR3}	MSAVI	NDVI	B_{Red}	B_{NIR}	B_{SWIR3}	MSAVI	NDVI	B_{Red}	B_{NIR}	B_{SWIR3}	MSAVI	NDVI
κ		0.80	0.85	0.10	**0.92**	**0.92**	0.59	0.78	0.08	**0.86**	**0.86**	0.79	0.85	0.08	**0.91**	**0.91**
κ (%)		35.5	8.9	25.0	6.9	6.9	-	-	-	-	-	33.8	8.9	0.0	5.8	5.8
McN.		442	135	15	114	185	-	-	-	-	-	389	128	25	119	258
UA (%)		90.8	92.8	49.0	96.0	96.2	80.6	89.5	46.3	93.5	93.7	90.2	92.8	59.6	95.7	96.0
PA (%)		90.6	92.2	48.8	96.2	96.3	80.6	88.9	45.1	93.4	93.5	90.2	92.2	63.6	95.7	95.7
OA (%)		90.5	92.5	52.0	96.0	96.1	80.2	89.1	49.8	93.3	93.4	90.0	92.4	58.7	95.6	95.8
Opt. Param.	I	100	22	27	8	9	-	-	-	-	-	8	21	100	16	17
	C	10	9	8	6	7	4	9	6	8	5	10	9	3	8	7
	RC	4	3	3	3	3	2	3	2	4	2	4	3	2	4	3

Table 7. 3rd Disctric: Villablino, Mine Feixolín (see Section 5.2 for detailed description)

		Best κ										Optimal Time				
		Filtered					Non Filtered									
Indexes		B_{Red}	B_{NIR}	B_{SWIR3}	MSAVI	NDVI	B_{Red}	B_{NIR}	B_{SWIR3}	MSAVI	NDVI	B_{Red}	B_{NIR}	B_{SWIR3}	MSAVI	NDVI
κ		0.86	0.75	0.57	**0.91**	0.89	0.82	0.68	0.50	**0.87**	0.86	0.80	0.75	0.53	**0.83**	0.82
κ (%)		4.8	10.2	14.0	4.5	3.4	-	-	-	-	-	-2.5	10.2	6.0	-4.6	-4.7
McN.		99	196	105	22	46	-	-	-	-	-	85	198	125	51	367
UA (%)		93.5	88.2	79.8	95.6	94.8	91.7	85.0	76.3	93.8	93.6	91.0	88.1	79.0	92.0	91.6
PA (%)		93.5	88.2	79.4	95.8	95.1	92.2	85.3	75.9	94.4	94.1	91.0	88.1	79.0	94.3	92.1
OA (%)		93.3	87.8	79.1	95.6	94.8	91.7	84.6	75.7	93.9	93.6	90.6	87.7	78.4	92.0	91.6
Opt. Param.	I	7	78	3	3	4	-	-	-	-	-	41	87	94	47	55
	C	6	8	5	7	8	8	8	4	9	8	6	8	9	4	9
	RC	3	2	2	3	3	4	2	2	4	3	3	2	4	2	4

5.3 Comments on the numerical results

The large amount of experiments carried out for the present work over a wide range of values for each parameter, allows us to draw several and interesting conclusions.

First of all it can observed that all of κ values of filtered inputs are improved if compared to the non filtered ones (with the same C and RC), and even if compared to the best of non filtered ones (i.e. even for different values of R and RC), and if compared to the results reached for the optimal iterations.

Moreover, the results in Tables 1-4 for filtered inputs outperform as well the results in [11] where a nonlocal and linear filter was considered instead of the local and nonlinear considered in the present . If we add the dramatic runtime reduction achieved by the present model, the convenience of these procedure keeps even clearer.

In most cases the best κ is reached before the optimal time, so we can conclude that optimal time, as computed in (8), stands for a threshold for the best κ, or in other words in view of practical results the best κ is expected to be reached long before the optimal time. Note that in most favorable cases (see Figures 5-6) the optimal time is reached for a short number of steps. Note also that the poor behavior of the optimal time, according Definition 8, is driven for the low inter–class variance that typically characterizes this kind of images, and makes the norm $\|U^m - \bar{U}^m\|_F$ to take small values. Consequently the correlation becomes larger, and the optimal time as well.

Moreover, it can be visually observed that data provided by the best κ outperform the ones achieved for the optimal time, and of course the ones achieved without any previous filtering. In fact, note that optimal time provide much worse results under some critical size of the affected area (Figures 1–2).

Finally, related to the classes and re–classes, no clear patterns have been found for the best results achievement. However it can be observed that in most cases the best results are achieved for a few time steps, number of classes close to 10, and a few number of classes.

6 Conclusions and future works

Our study has shown that the accuracy of degraded (burned/surface coal affected) are maps is notably higher when the proposed PDE's based filter is applied if compared to the accuracy of the scheme without filtering. In addition, since the best results were obtained in a short number of steps, it makes their implementation feasible in practical instances. Moreover since most times the best results were obtained before the optimal time for the filtering process is reached, one can consider the optimal time as a heuristic benchmark for the number of iterations.

In the near future we expect to achieve real optimizations of results in terms of the parameters involved in the procedure, in particular for affected areas of small size whose patterns keep not clear at all in view our experimental results.

Acknowledgements The first author was supported by the Spanish Ministry of Science, Innovation, and Universities (project RTI2018-094569-B-I00), and the two second authors by the Spanish Ministry of Economy and Competitiveness (FIRE-SEVES project, 559 AGL2017-86075-C2-1-R), and the Regional Government of Castilla y León (Spain) (SEFIRECYL project, LE001P17).

References

1. Araújo, A., Barbeiro, S., Cuesta, E., Durán, A.: Cross–diffusion systems for image processing: I. the linear case. J. Math. Imaging Vis. **58**(3), 447–467 (2017)
2. Araújo, A., Barbeiro, S., Cuesta, E., Durán, A.: Cross–diffusion systems for image processing: II. The nonlinear case. J. Math. Imaging Vis. **58**, 427–446 (2017)
3. Araújo, A., Barbeiro, S., Serranho, P.: Stability of finite difference schemes for complex diffusion processes. SIAM J. Numer. Anal. **50**, 1284–1296 (2012)
4. Aubert, G., Kornprobst, P.: Mathematical Problems in Image Processing. Partial Differential Equations and the Calculus of Variations, *Applied Mathematical Sciences*, vol. 147. Springer-Verlag New York (2006)
5. Aurich, V., Weule, J.: Non–linear gaussian filters performing edge preserving diffusion. Sagerer G., Posch S., Kummert F. (eds) Mustererkennung 1995. Informatik aktuell. Springer, Berlin, Heidelberg pp. 538–545 (1995)
6. Buades, A., Coll, B., Morel, J.M.: The staircasing effect in neighborhood filters and its solution. IEEE Transactions on Image Processing **15**(6), 1499–1505 (2006)
7. Camia, A., San-Miguel-Ayanz, J., Oehler, F., de Oliveira, S.S., Durrant, T., Kucera, J., Boca, R., Whitmore, C., Giovando, C., Amatulli, G., Libertá, G., Schmuck, G., Schulte, E., Bucki, M.: Forest Fires in Europe 2008. Technical Report. Tech. rep., Luxembourg: Joint Research Centre – Institute for Environment and Sustainability, Office for Official Publications of the European Communities (2009)
8. Catté, F., Lion, P.L., Morel, J.M., Coll, T.: Image selecting smoothing and edge detection by nonlinear diffussion. SIAM J. Numer. Anal. **129**, 182–193 (1992)
9. Chuvieco, E., Martín, M., Palacios, A.: Assessment of different spectral indexes in the red–near–infrared spectral domain for burned land discrimination. Int. J. Remote Sens. **23**, 5103–5110 (2002)
10. Congalton, R.G., Green, K.: Assessing the Accuracy of Remotely Sensed Data: Principles and Practice. Boca Raton: CRC press (Taylor & Francis) (2009)
11. Cuesta, E., Quintano, C.: Linear fractional–based filter as a pre–classifier to map burned areas in mediterranean countries. Int. J. Remote Sens. **36**, 3293–3316 (2015)
12. Dietterich, T.: Approximate statistical test for comparing supervised classification learning algorithms. Neural Comput. **10**, 1895–1923 (1998)

13. Edwards, A., Maier, S., Hutley, L., Williams, R., Russell-Smith, J.: Spectral analysis of fire severity in north Australian tropical savannas. Remote Sens. of Environ. **136**, 56–65 (2013)
14. Fernández-Manso, A., Quintano, C., Roberts, D.: Evaluation of potential of multiple endmember spectral mixture analysis (MESMA) for surface coal mining affected area mapping in different world forest ecosystems. Remote Sens. of Environ. **127**, 181–193 (2012)
15. Galiano, G., Garzón, M.J., Jüngel, A.: Analysis and numerical solution of a nonlinear cross–diffusion system arising in population dynamics. Rev. R. Acad. Cie. Ser. A Mat. **95**(2), 281–295 (2001)
16. Galiano, G., Garzón, M.J., Jüngel, A.: Semi-discretization in time and numerical convergence of solutions of a nonlinear cross–diffusion population model. Numer. Math. **93**, 655–673 (2003)
17. García-Criado, F., Tome, A., Vega, F.J., Antolín, C.: Performance of some diversity and biotic indices in rivers affected by coal mining in northwestern Spain. Hydrobiologia **394**, 209–217 (1999)
18. Gilboa, G., Zeevi, Y.Y., Sochen, N.A.: Complex diffusion processes for image filtering. In: M. Kerckhove (ed.) Scale-Space and Morphology in Computer Vision, vol. Third International Conference, Scale-Space 2001, Vancouver, Canada, July 7-8, Springer, Berlin. Proceedings, pp. 299–307 (2001)
19. Hoscilo, A., Tansey, K., Page, S.: Post–fire vegetation response as a proxy toquantify the magnitude of burn severity in tropical peatland. Int. J. Remote Sens. **34**, 412–433 (2013)
20. Huang, Y., Tian, F., Wang, Y., Wang, M., Hu, Z.: Effect of coal mining on vegetation disturbance and associated carbon loss. Environ. Earth. Sci. **73**(5), 2329–2342 (2014)
21. Huete, A., Liu, H., Batchily, K., van Leeuwen, W.: A comparison of vegetation indices over a global set of TM images for Eos–Modis. Remote Sens. of Environ. **59**, 440–451 (1997)
22. Huete, A.R.: A soil–adjusted vegetation index (SAVI). Remote Sens. of Environ. **25**, 295–309 (1988)
23. Kaplan, N., Erer, I., Gulmus, N.: Remote sensing image enhancement via bilateral filtering. In: 2017 8th International Conference on Recent Advances in Space Technologies (RAST) (2017)
24. Key, C.H., Benson, N.: Landscape assessment: Sampling and analysis methods: Firemon: Fire effects monitoring and inventory system. General Technical Report. Tech. rep., USDA Forest Service, Rocky Mountain Research Station, Fort Collins CO., RMRS-GTR-164-CD (2006)
25. Lechner, A.M., Baumgartl, T., Matthew, P., Glenn, V.: The impact of underground longwall mining on prime agricultural land: A review and research agenda. Land Degrad. Dev. **27**(6), 1650–1663 (2014)
26. Lloyd, S.P.: Least square quantization in pcm. IEEE Transactions on Information Theory. **28**(2), 129–137 (1957)
27. Lloyd, S.P.: Least squares quantization in pcm. IEEE Trans. Inf. Theory **28**, 129–137 (1982)
28. López-García, M., Caselles, V.: Mapping burns and natural reforestation using thematic mapper data. Geocarto International **6**, 31–37 (1991)
29. Lorenz, D.A., Bredies, K., Zeevi, Y.Y.: Nonlinear complex and cross–diffusion (2006). Unpublished report, University of Bremen. Freely available in: https://www.researchgate.net
30. Martín, M., Gómez, I., Chuvieco, E.: Performance of a Burned Area Index (BAIM) for mapping Mediterranean burned scars from MODIS data. In Proceedings of the 5th International Workshop on Remote Sensing and GIS Applications to Forest Fire Management: Fire Effects Assessment, Zaragoza (Spain) pp. 193–198 (2005)
31. Miller, J.D., Knapp, E.E., Key, C.H., Skinner, C.N., Isbell, C.J., Creasy, R.M., Sherlock, J.W.: Calibration and validation of the relative differenced normalized burn ratio RdNBR to three measures of fire severity in the Sierra Nevada and Klamath Mountains, California, USA. Remote Sens. of Environ. **113**, 645–656 (2009)
32. Mrázek, P., Navara, M.: Selection of optimal stopping time for nonlinear diffusion filtering. Int.l J. Comput. Vis. **52**(2), 189–203 (2003)
33. Ni., W.M.: Diffusion, cross–diffusion and their spike–layer steady states. Notices AMS **45**(1), 9–18 (1998)
34. Paris, S., Kornprobst, P., Tumblin, J., Durand, F.: A gentle introduction to bilateral filtering and its applications. In: U. ACM New York NY (ed.) SIGGRAPH '07. ACM SIGGRAPH 2007 courses (2007)
35. Pereira, J.M.: A comparative evaluation of NOAA/AVHRR vegetation indexes for burned surface detection and mapping. IEEE Trans. Geosci. Rem. Sensing **37**, 217–226 (1999)
36. Perona, P., Malik, J.: Scale space and edge detection using anisotropic diffusion. Proc. IEEE Comp. Soc. Workshop on Computer Vision - Miami Beach, Nov. 30 – Dec. 2 pp. 16–22 (1987)
37. Perona, P., Malik, J.: Scale–space and edge detection using anisotropic diffusion. IEEE Trans. Pattern Anal. Mach. Intell. **12**, 629–639 (1990)
38. Qi, J., Kerr, Y., Chehbouni, A.: External factor consideration in vegetation index development. In: CNES, Proceedings of 6th International Symposium on Physical Measurements and Signatures in Remote Sensing, pp. 723–730 (1994b)
39. Quintano, C., Cuesta, E.: Improving satellite image classification by using fractional type convolution filtering. Int. J. Appl. Earth. Obs. **12**, 298–301 (2010)
40. Schmuck, G., San-Miguel-Ayanz, J., Camia, A., Durrant, T., Boca, R., Whitmore, C., Libertá, G., Corti, P.: Forest Fires in Europe, Middle East and Norh Africa, 2011. Tech. rep., Ispra: Joint Research Centre and Directorate–General Environment (2012)
41. Stehman, S.V.: Altmetric original articles sampling designs for accuracy assessment of land cover. Int. J. Remote Sens. **30**(20), 5243–5272 (2009)
42. Tucker, C.J.: Red and photographic infrared linear combinations for monitoring vegetation. Remote Sens. of Environ. **8**, 127–150 (1979)
43. Weickert, J.: Anisotropic Diffusion in Image Processing. B.G. Teubner, Stuttgart (1998)
44. Ya-Lin, H., Zhi-Xin, N., De-Hui, Z., 26, W.C.Y.: Soil amendment improves tree growth and soil carbon and nitrogen pools in mongolian pine plantations on post–mining land in northeast china. Land Degrad. Dev. **26**, 807–812 (2015)
45. Zhao, W.L., Deng, C.H., Ngo, C.W.: k-means: A revisit. Neurocomputing **291**, 195–206 (2018)

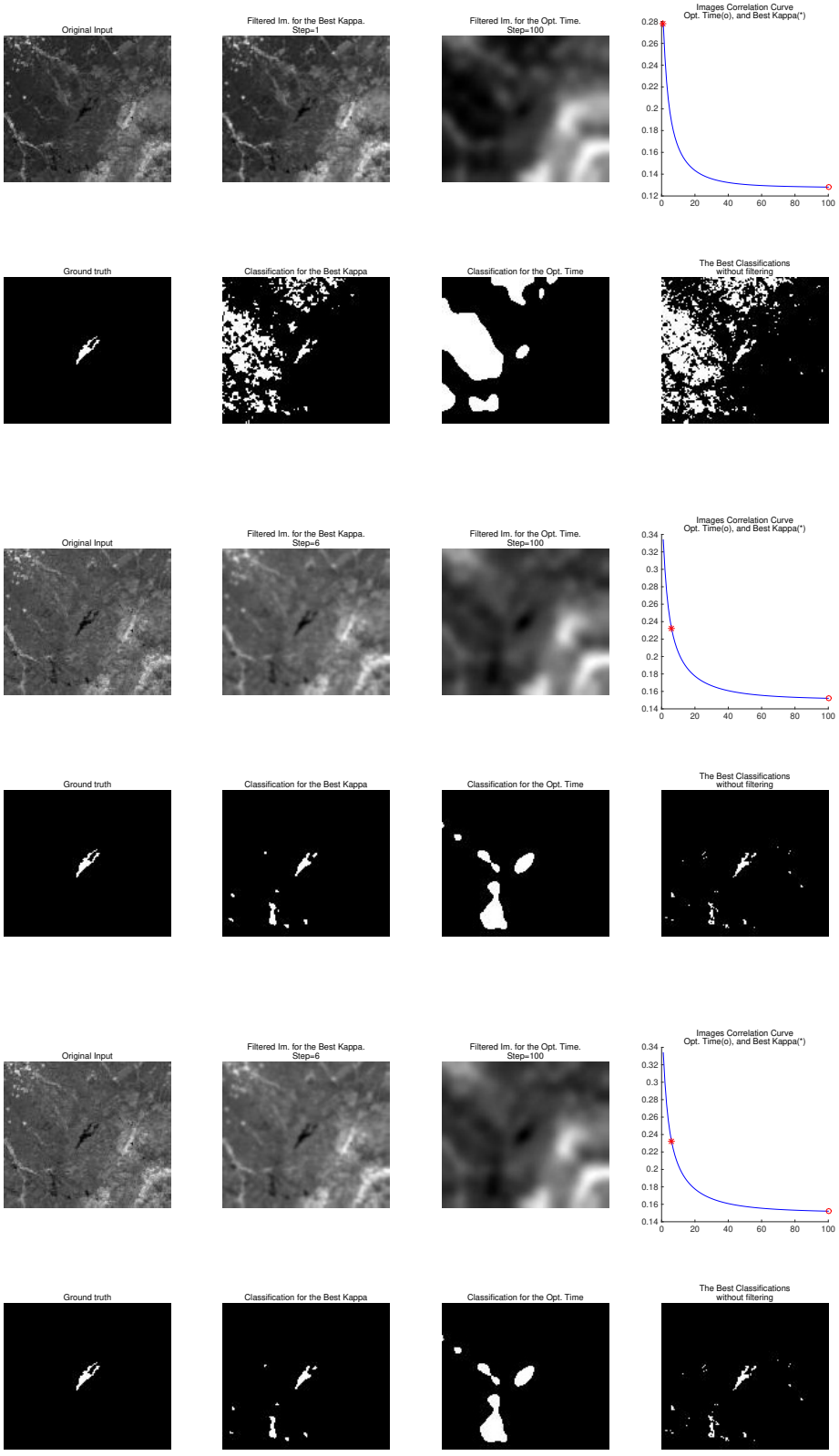

Fig. 1 2nd Forest fire, Zamora (2): EVI (rows 1 and 2), GEMI (rows 3 and 4), BAI (rows 5 and 6)

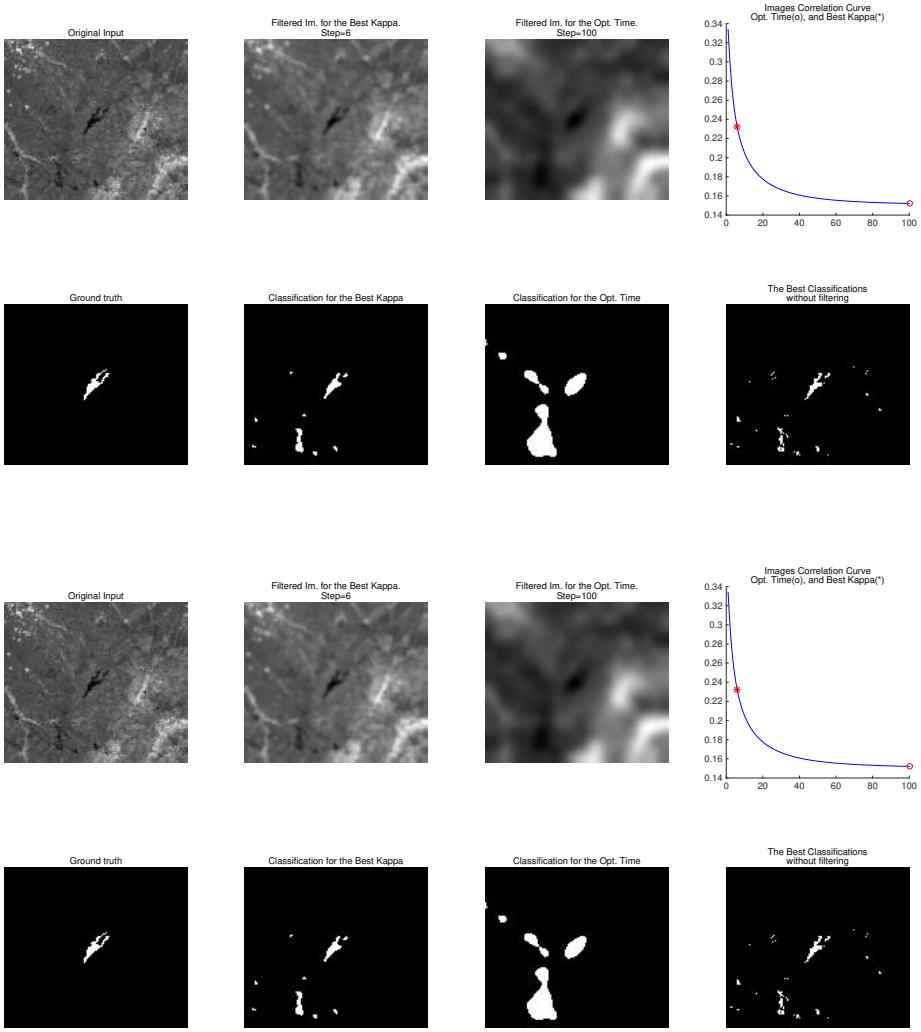

Fig. 2 2nd Forest fire, Zamora (2): BAIM (rows 1 and 2), NBR (rows 3 and 4)

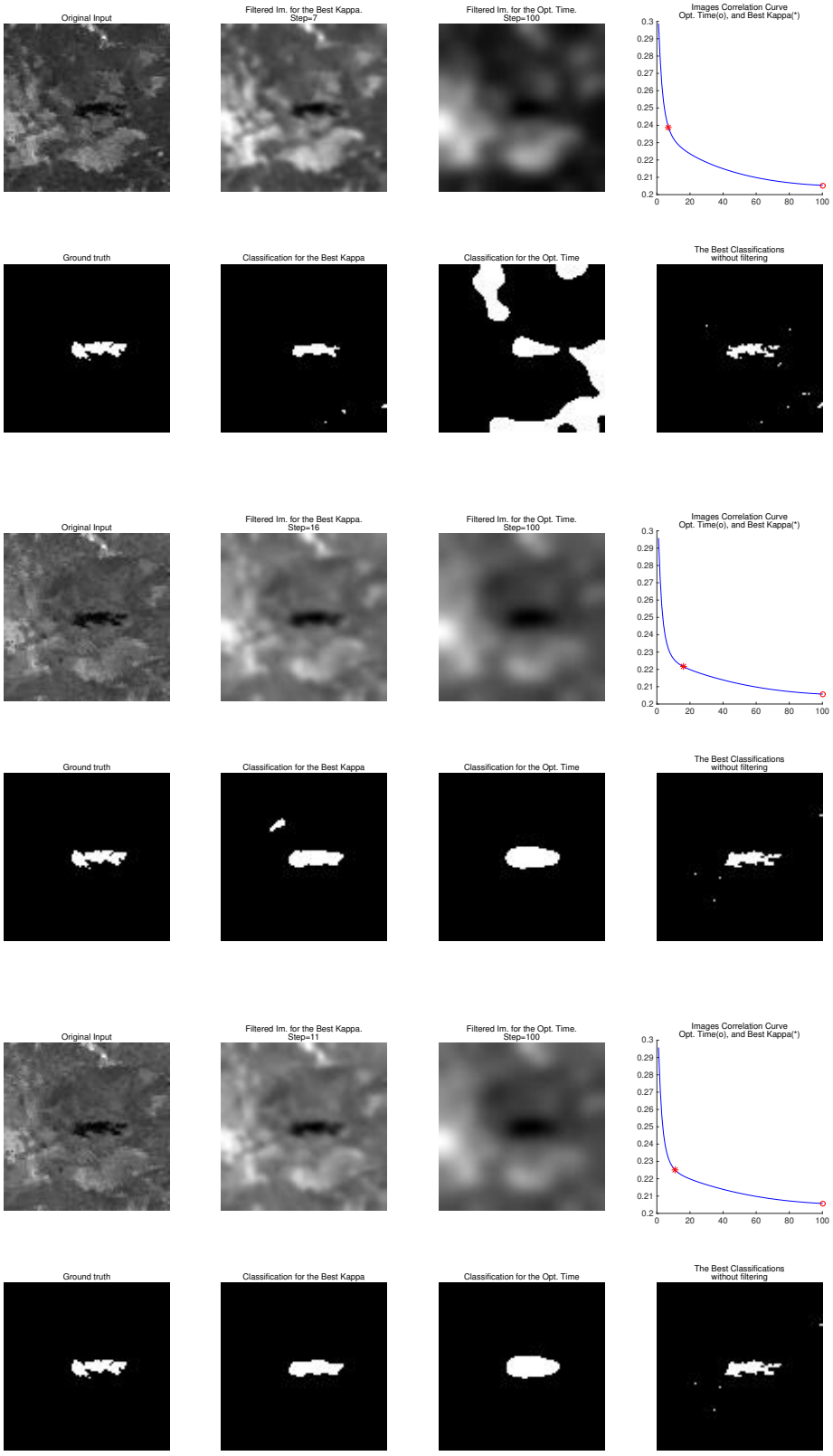

Fig. 3 3rd Forest fire, Burgos: EVI (rows 1 and 2), GEMI (rows 3 and 4), BAI (rows 5 and 6)

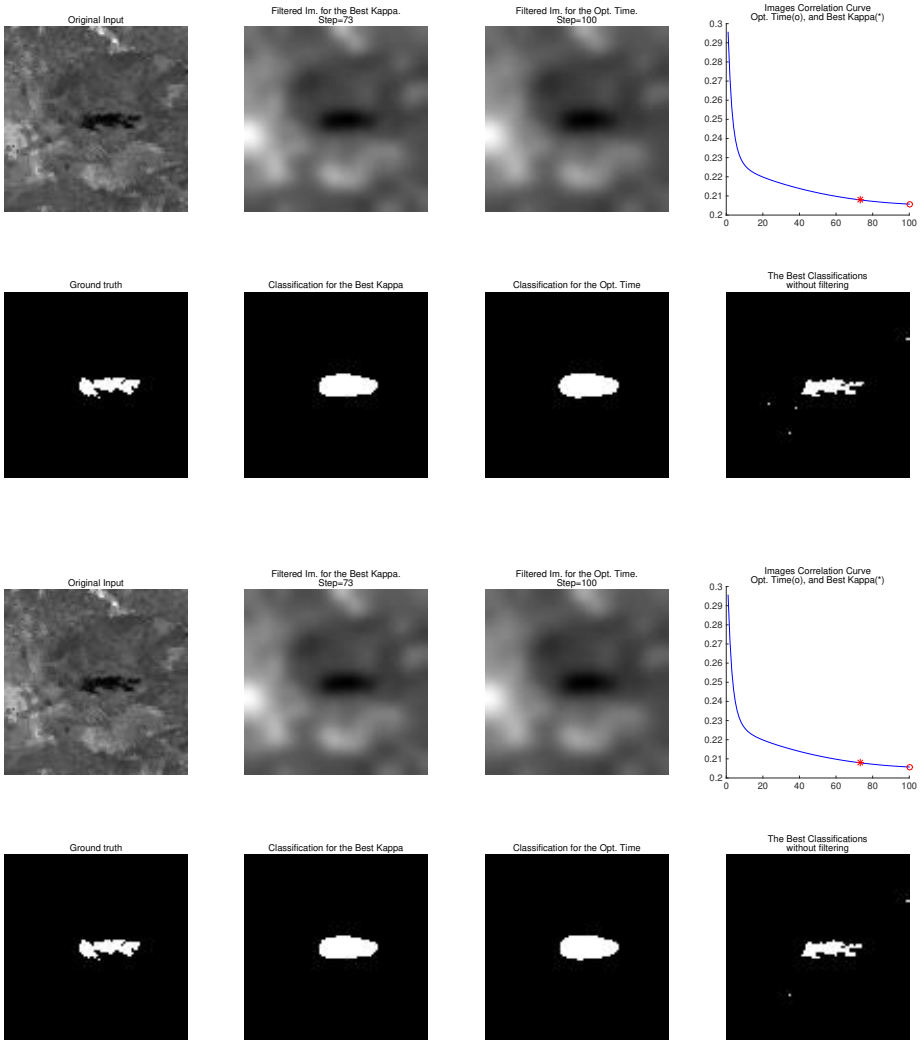

Fig. 4 3rd Wildfire, Burgos: BAIM (rows 1 and 2), NBR (rows 3 and 4)

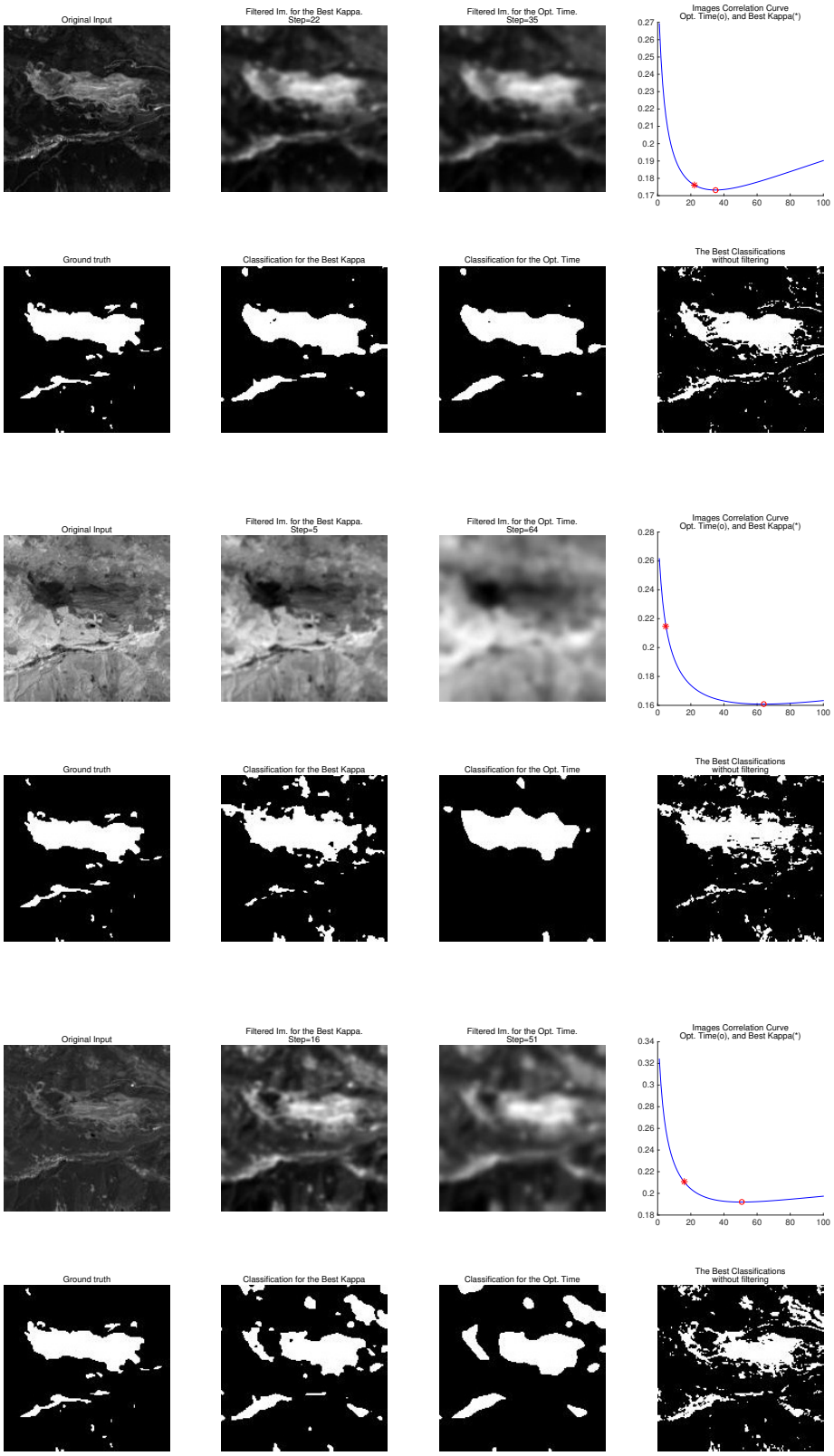

Fig. 5 1st Coal, Cerredo:B_{Red} (rows 1 and 2), B_{NIR} (rows 3 and 4), B_{SWIR3} (rows 5 and 6)

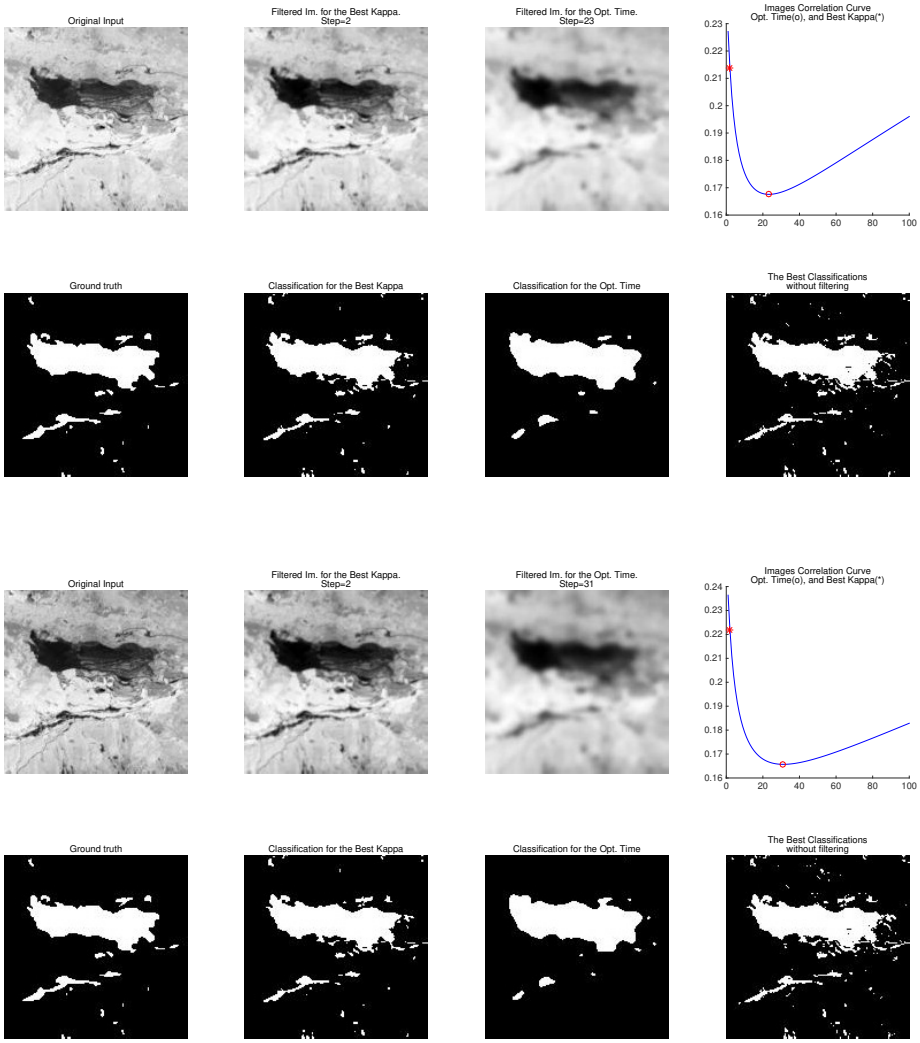

Fig. 6 1st Coal, Cerredo: MSAVI (rows 1 and 2), NDVI (rows 3 and 4)